Oceanic Bubble Population Measurements Using a Buoy-Deployed Combination Frequency Technique

Andy D. Phelps and Timothy G. Leighton

Abstract— **This paper presents the results of using a combination frequency acoustic technique to measure the near-surface bubble population in the open sea. The combination frequency technique monitors the appearance of sum-and-difference signals generated by the nonlinear interaction of two sound fields: one, a high-frequency signal, scatters geometrically from the bubble, and the other, of much lower frequency, is used to excite the bubble into resonant pulsation. The text details the calibration of the apparatus necessary to relate the measured heights of the sum-and-difference terms to actual numbers of bubbles and describes the experimental procedure for the collection of the oceanic data. In total, six trials were performed over a one-day period, each comprising ten "snapshots" of the local bubble population at ten discrete radii. This data was augmented with simultaneous video, slide, and dictaphone records of the state of the sea around the measurement position.**

Index Terms— **Bubbles, nonlinear oscillators, sea measurements, sea surface, underwater acoustic measurements.**

I. INTRODUCTION

IT HAS BEEN known for some time [1] that bubbles are an important source of ambient sound in the oceans and are also known to contribute a significant asymmetry to the transport of greenhouse gases across the atmosphere/ocean boundary [2], [3]. Thus, a reliable and unambiguous technique for measuring the local bubble population would be of benefit to the modeling of such oceanographic processes.

The use of acoustics is especially practical in the measurement of a bubble population [4]. The significant impedance mismatch at the bubble surface between the gas inside and the surrounding liquid ensures that there is significant reflection of an insonifying sound field. Additionally, when driven acoustically at low amplitudes, bubbles behave approximately as single-degree-of-freedom oscillators. The gas inside contributes the stiffness element, the liquid outside the bubble behaves as the mass element, and the damping of the bubble pulsations is brought on through viscous losses at the bubble wall, radiation of acoustic energy into the medium, and thermal losses in the expansion and compression of the gas. The resonance frequency of these pulsations (ν_0) can be expressed in terms of the equilibrium radius (R_0) as

$$\nu_0 = \frac{1}{2\pi R_0 \sqrt{\rho}} \sqrt{3\kappa \left(p_0 + \frac{2\sigma}{R_0} \right) - \frac{2\sigma}{R_0} - \frac{4\mu^2}{\rho R_0^2}} \qquad (1)$$

where ρ is the density of the surrounding liquid, p_0 is the hydrostatic pressure at the bubble wall, σ is the surface tension coefficient at the gas–liquid interface, μ is the shear viscosity coefficient, and κ is the polytropic index describing the expansion and compression of the gas within the bubble. Therefore, from a knowledge of its resonant frequency, the size of the bubble can be determined.

The particular measurements described in these tests use a combination frequency technique to characterize the bubble population. Here, the bubble population is simultaneously insonified with two sound fields, a *pump* signal (at frequency ω_p) and an *imaging* signal (at frequency ω_i). The pump signal is of low amplitude, and its frequency is varied to coincide with the resonance frequencies of members of the bubble population under investigation (for these oceanic measurements, this ranged between 17 and 200 kHz at 1000 Pa amplitude). The imaging signal is considerably higher in frequency (here set at 1 MHz) and is used to continuously insonify the population. The high-frequency backscattered signal is then monitored. For a single bubble, this consists of the geometrically scattered imaging signal from the bubble, brought about by the impedance mismatch at the bubble wall. However, if the pump sound field is at or close to a bubble resonance, the bubble will be pulsating at this frequency, and the target area of the scatterer will be changing. Therefore, the scattered signal will be amplitude-modulated at the frequency of the pump signal, resulting in the generation of sum and difference signals at $\omega_i \pm \omega_p$. Thus, the technique monitors the linear resonant pulsation characteristics of a bubble through the generation of a nonlinear component in the returned signal.

The benefits of using a two-frequency technique over a single frequency insonification measurement are that the analysis of the returned signal allows less ambiguous and more accurate estimates of the measured population. When single-frequency linear backscatterers are employed [5], there is an ambiguity in the returned signal, as a large nonresonant bubble insonified by a high-frequency sound field may scatter more sound than that from a smaller resonant bubble. However, the height of the combination frequency signal at $\omega_i \pm \omega_p$ is a global maximum at the bubble resonance. This is shown in an earlier paper [6], where a large bubble is insonified by a pump signal three times higher in frequency than the bubble resonance: small sum-and-difference signals are generated, at amplitudes very close to the model predictions, demonstrating the potential to account for off-resonance scattering.

Additionally, there is a considerable improvement in the spatial localization of a bubble using this technique over

single-frequency insonification. At resonance, the wavelength of the insonifying sound field is much larger than the bubble radius; for example, a 1-mm-radius bubble in water at atmospheric pressure is resonant at approximately 3.2 kHz, whereas a 3.2-kHz plane wave has a wavelength of about 0.5 m. However, the insonifying volume of the combination frequency measurements is determined solely by the intersection of the high-frequency projector and receiver transducers and is therefore much smaller and can be readily calculated. A further benefit of the technique is that the modulation process translates only the relevant bubble-mediated information from the "noisy" frequency window around the resonance (due to the incident acoustic pump signal, bubble entrainment noise, etc.) to a much quieter window around the imaging frequency, thereby allowing an improved signal-to-noise ratio (SNR).

This paper describes measurements of the oceanic bubble population at the sea surface at high wind speeds (10–12 m/s), using this combination frequency technique. The number of bubbles at ten distinct radii ranging between 16 and 192 μm were estimated at a depth of 0.5 m. A similar setup was earlier employed to measure the population in the surf zone [7], but the calibration procedure is described here in detail as it is greatly improved from that employed in the earlier tests, and the procedure for analyzing the data is discussed. The oceanic apparatus and the experiment are then described, and the results of the tests presented. These are compared with historical measurements and differences in the bubble size spectra discussed.

II. HISTORICAL OCEANIC BUBBLE MEASUREMENTS

There are four notable measurements of the ocean population recorded near the surface (<1.5 m) in deep water (using an oceanographic definition, described later) in high wind speeds (11–15 m/s), and these will be used later for comparison with the data collected using this combination frequency technique. Other notable measurements of bubble populations have been made in more shallow water (for example, the sound speed and attenuation inversions employed by Melville *et al.* [8] at 6.5-m depth inshore of the surf line), but these are therefore not directly comparable with the measurements presented here.

The earliest oceanic bubble population measurements were performed by Johnson and Cooke [9] who employed a sophisticated optical measurement technique in 20–30-m-deep water. Their data for 0.7-m depth and 11–13-m/s wind speed is shown in Fig. 1, where it is compared with other historical measurements which are described below. Their data shows a steady increase in the population between ∼200- and 60-μm radii, which then flattens out until approximately 20 μm. However, other workers have commented that the photographic observations lack the necessary resolution to observe these smaller bubbles, and that the measured population may underestimate the actual population [10].

These optical measurements were followed by an acoustic technique of Farmer and Vagle [5] which used four upwardly facing sonar transducers and monitored the linear backscatter at the four frequencies 28, 50, 88, and 200 kHz. The data was used to infer an ambient bubble population which was then
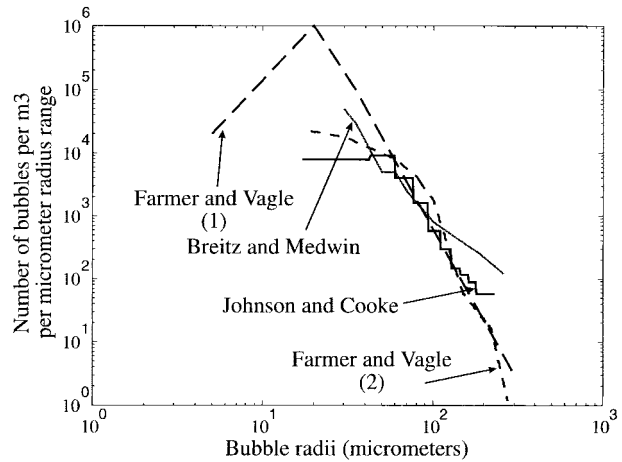

Fig. 1. Comparison of four historical measurements of the near-surface bubble population in deep water and at high wind speed. The data is taken from [9] (black unbroken), [6] [large dashes], [11] (grey unbroken), and [12] [small dashes].

used in modeling the waveguide propagation characteristics in the bubble layer. The population estimates inferred from the strength of the backscattered signal wave were iteratively matched to the Johnson and Cooke optical data at large bubble size. The estimated population is also shown in Fig. 1, taken at 10-cm depth and in 12–14 m/s wind speed from the Fasinex location, and shows the population to rise up to a maximum at 20 μm of around 1×10^6 bubbles per m^3 per 1-μm-radius increment.

The third notable historical measurement was performed by Breitz and Medwin [11], who used a flat plate resonator to characterize the local oceanic population. This technique again relies on the (assumed) linear bubble behavior to affect the attenuation of modes set up between the two resonator plates, which can be used to infer population numbers for bubbles resonant at those modal frequencies. The technique can yield absolute measures of the bubble population, and their measurements are shown in Fig. 1 with the other three historical estimates. This data was collected at 25 cm below the sea surface in 120-m water depth in a 12-m/s wind speed. Their data shows a monotonically increasing bubble population between 250 and 30 μm, but with a higher number of larger bubbles than the other two estimates and a slightly reduced number of smaller bubbles than those estimated by Farmer and Vagle [5].

A fourth measurement of the oceanic population is presented again by Farmer and Vagle [12], who themselves employed an acoustic resonator, but with a larger radius span than the earlier Breitz and Medwin experiment. Their data was taken at a lower depth of 1.3 m, although in wind speeds comparable with the other data shown (10 m/s). Typical results are shown in Fig. 1 with the other historical measurements. The data shows good agreement with the earlier workers for bubbles larger than 40 μm, and then dips off to fall between the Breitz and Medwin data and that of Johnson and Cooke for smaller bubbles. This may be due to the greater depth at which the recent Farmer and Vagle population was measured, or a limitation of their measurement technique. The workers calibrate their data by

using their measured population to calculate the sound-speed anomaly due to the presence of the bubbles, and compare this directly with measured sound-speed data. The agreement is excellent for larger bubbles, but at the smallest bubble sizes there is a divergence between the measured value and predicted estimate.

Combination frequency measurements have been employed by earlier workers sizing bubbles in the laboratory using increasingly more sophisticated signal processing techniques [13]–[15] and once on an oceanic population [16]. However, the latter tests were concerned only with bubbles resonant between 2.5 and 6 kHz, whereas to fully characterize the ambient population it is necessary to investigate bubbles up to approximately 200 kHz [12], [17]. The workers used a chirped signal as their pump source and an imaging frequency of 450 kHz. In addition, no distinction was made in their tests between bubble-mediated signal coupling and that caused by turbulence and direct reflection of the imaging signal off the moving pump transducer face plate. As will be shown, the contribution to the sum-and-difference signal from this direct coupling is significant, and care must be taken to distinguish and remove this effect from the bubble count. Additionally, the large off-resonant nature of the $\omega_i \pm \omega_p$ signal was ignored by Koller *et al.* [16]. It is important to include this since the volumetric pulsation resonance of a bubble has a significant Q value. Also, Koller *et al.* did not compensate for the variable frequency response of the pump transducer, a necessary step if the amplitude of the sum-and-difference signal components is to be related to bubble numbers.

Since then, the combination frequency technique has been successfully employed to measure the population in the surf zone at a depth of 1.5 m at four distinct pump frequencies—28, 50, 60, and 88 kHz, using a more robust estimation and calibration technique [7]. The results indicate a local population more than two orders of magnitude higher than any of the deep-water measurements, as a result of the differences in wavebreaking activity in the shallow water.

III. CALIBRATION TECHNIQUES

A. Bubble Response to Two-Frequency Insonification

It is preferable for a generalized bubble sizer to be able to obtain an absolute measure of the population, rather than relying on existing data as a starting point for an interpolation procedure. The procedure for translating the measured spectral levels into an absolute bubble count are outlined below and involves employing a suitable model for the bubble pulsation response to two-frequency insonification.

The calibration procedure is as follows. A stream of single-size rising bubbles was insonified in the laboratory using the same apparatus as would be later employed in the sea trials. Using an identical experimental setup for both sets of tests enables several parameters in the pulsation modeling to be poorly defined without any loss of accuracy in the eventual calculations, such as the amplitude of the imaging signal and the distance between the receiver transducer and the transducer focus. Having obtained measured voltage levels for the various spectral components of the returned signal, the

same insonification conditions as those used in the experiments were modeled to estimate the expected sound pressure levels at the different returned signal frequencies. A comparison between the measured and modeled signal heights allows a transfer function relating the measured voltage levels to the actual number of bubbles to be estimated. The modeled signal heights for the ten frequencies used in the sea trials were then estimated (using parameters relevant to sea water). These were then used, along with the estimated transfer function and measurements of the frequency response of the components in the returned signal line, to obtain bubble population estimates from measured two-frequency backscattered signal levels.

Earlier workers who analytically derived expressions for the height of the sum-and-difference terms [13], [18] used simplified forms of the Rayleigh–Plesset equation to obtain expressions for the pressure amplitudes at the various frequency locations. However, they took account only of viscous damping of the bubble motion, which for the bubbles in question is an order of magnitude smaller than damping through thermal and radiation losses [19] (although it should be noted that Newhouse and Shankar [13] made the damping an unknown variable which they optimized to give best fit between their measured data and the bubble counts they expected). The algorithm for interpreting acoustic data in terms of bubble counts used in this paper uses a more appropriate model of the bubble pulsation characteristics based on the formulations derived by Herring [20] and Keller [21]. It can be written as

$$\left(1 - \frac{\dot{R}}{c}\right) R\ddot{R} + \frac{3}{2}\dot{R}^2\left(1 - \frac{\dot{R}}{3c}\right)$$
$$= \left(1 + \frac{\dot{R}}{c}\right)\frac{1}{\rho}\left[p_B(t) - p_0 - p\left(t + \frac{R}{c}\right)\right]$$
$$+ \frac{R}{\rho c}\frac{dp_B(t)}{dt}. \tag{2}$$

In addition to the symbols defined earlier, R is the instantaneous bubble radius, with its two derivatives with respect to time indicated with dots above the character, c is the speed of sound in the fluid, and $p(t)$ is the driving acoustic pressure. The remaining term $p_B(t)$ is a measure of the pressure immediately outside the bubble wall and represents the forcing term on the liquid due to the bubble which the acoustic pressure has to overcome. It is given by

$$p_B(t) = \left(p_0 + \frac{2\sigma}{R_0}\right)\left(\frac{R_0}{R}\right)^{3\kappa} - \frac{2\sigma}{R} - \frac{4\mu\dot{R}}{R}. \tag{3}$$

Although it is possible to solve (2) and (3) numerically for each specific bubble insonification case, a small approximation allows an analytical solution. This is achieved by considering the pulsations to be small amplitude [22]. The variable R can thereby be rewritten in terms of a small radial perturbation variable x as

$$R = R_0(1 + x), \qquad \text{with } x \ll 1. \tag{4}$$

Using this substitution, it is possible to rewrite (2) and (3), where all terms beyond those in x^2 are neglected, as (5), shown at the bottom of the next page. The subsequent analysis
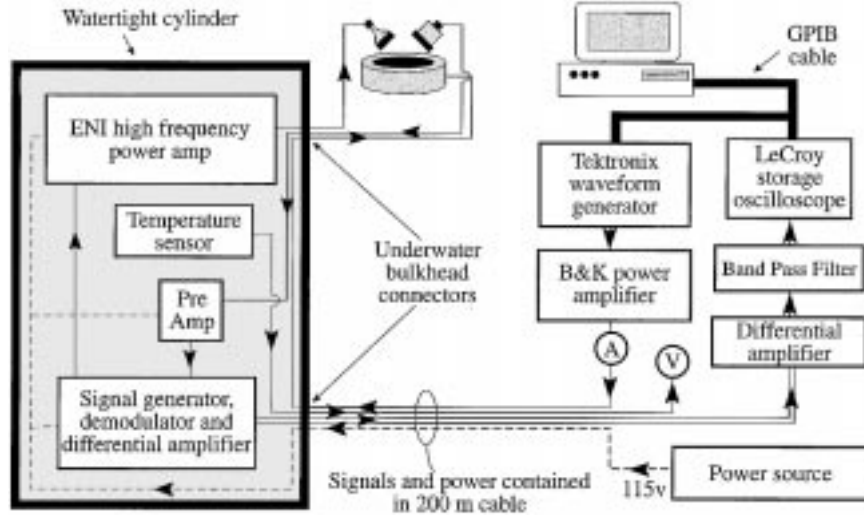
Fig. 2. Schematic of the apparatus used in both the laboratory and oceanic measurements.

involves first writing a solution to the displacement variable x in terms of a sum of radial excursions at the six frequencies, as

$$x = \tilde{A}_0 + \tilde{A}_1 e^{j\omega_p t} + \tilde{A}_2 e^{j\omega_i t} + \tilde{A}_3 e^{j2\omega_p t} + \tilde{A}_4 e^{j2\omega_i t}$$
$$+ \tilde{A}_5 e^{j(\omega_i + \omega_p)t} + \tilde{A}_6 e^{j(\omega_i - \omega_p)t} \quad (6)$$

where $\tilde{A}_1$, $\tilde{A}_2$, etc., are the complex amplitudes of the radial excursions at each frequency. This solution can then be substituted into the modified small amplitude Herring–Keller equation (5). Retaining only cross terms in $\tilde{A}_1^2$, $\tilde{A}_2^2$, and $\tilde{A}_1\tilde{A}_2$, an expression for the signal heights at the various different frequencies can be equated. This analytical solution is readily obtained, but it cannot be simplified to obtain a transparent expression in the same manner in which earlier workers reduced their formulations based on the Rayleigh–Plesset model [13] and is therefore not presented here.

Because this refined analysis allows for a finite speed of sound in the medium, rather than assuming the surrounding liquid to be incompressible [13], it explicitly allows for energy losses through acoustic radiation into the medium. By incorporating a polytropic relationship which relates the pressure of the gas inside the bubble to the radius, rather than the earlier assumed adiabatic relationship [13], the thermal damping losses are also considered. The value of κ is calculated theoretically using the expressions of Eller [19].

B. Laboratory Calibration

The equipment schematic is shown in Fig. 2 for the oceanic tests. To ensure that any potential signal corruption was iden-

tified and compensated for, the laboratory tests deployed the apparatus exactly as it would later be used in the oceanic tests, although without the equipment canister (described later), but at the same anticipated transducer depth of 50 cm. The hardware is described elsewhere [7], although as the deployment, control, and calibration details differ slightly, they will be discussed below. The frequency response of the pump transducer was previously calibrated over the frequency range employed in all the tests allowing constant and known insonification conditions to be employed.

The sensing volume was calculated by modeling the beam patterns of the two high-frequency transducers by performing a Rayleigh integral over their surfaces. When these patterns were overlapped in the same layout as the transducer arrangement, they allowed the insonification volume to be estimated. This gave a volume, defined by where the sensitivity fell off to 3 dB of its maximum value, of 1.0 cm^3 (the error in this estimate will be discussed in Section VI). The result of such a procedure for the employed transducer geometry is shown in Fig. 3, where the distance between both the high-frequency transducers and the focus is 16 cm and both transducers are angled at 45° to the vertically rising bubble flow.

The historical manner for presenting the bubble population information is as the number of bubbles at a particular bubble radius per cubic meter of water per micrometer radius range. Thus, it is important to be able to determine the radius range over which the sum-and-difference signals persist, so this can be compensated for in the analysis. This was again achieved through the Herring–Keller simulations, where the radial width

$$\left(1 - \frac{R_0 \dot{x}}{c}\right) R_0^2 \ddot{x}(1+x) + \frac{3}{2} R_0^2 \dot{x}^2 \left(1 - \frac{R_0 \dot{x}}{3c}\right)$$
$$= \left(1 + \frac{R_0 \dot{x}}{c}\right) \frac{1}{\rho} \left[\left(p_0 + \frac{2\sigma}{R_0}\right)\left(1 - 3\kappa x + \frac{3\kappa(3\kappa+1)x^2}{2}\right) - \frac{2\sigma}{R_0}(1 - x + x^2) - 4\mu\dot{x}(1-x) - p_0 - p(t) \right]$$
$$+ \frac{R_0(1+x)}{\rho c}\left\{ \dot{x}\left[\left(p_0 + \frac{2\sigma}{R_0}\right)(-3\kappa + 3\kappa(3\kappa+1)x) - \frac{2\sigma}{R_0}(-1 + 2x) \right] + 4\mu\left(x\ddot{x} + \dot{x}^2 - \ddot{x}\right) \right\} \quad (5)$$
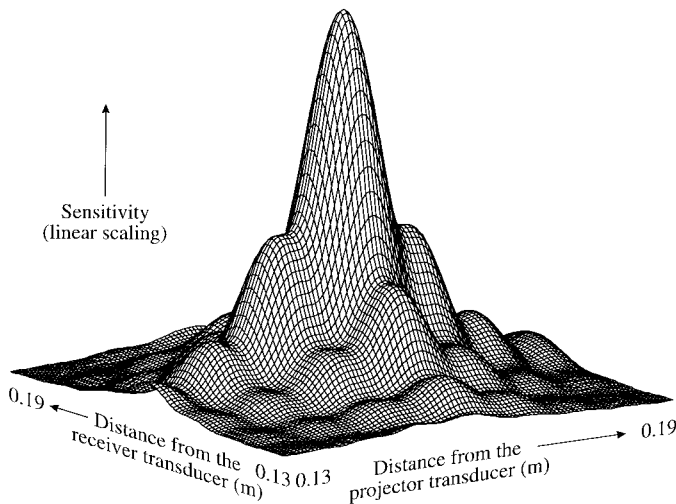
Fig. 3. Mesh plot of the sensitivity function within the high-frequency transducer sampling volume.

of each sum-and-difference peak was taken as the radius span before the signal height dropped by 3 dB.

IV. RESULTS OF LABORATORY TESTS

A steady stream of similar size bubbles was used in the laboratory tests, generated by passing compressed air through a hypodermic needle which had been constricted at the tip (the large pressure drop at the tip ensured that the bubbles would all be the same size [23]). Fig. 4(a) shows a typical returned signal from the insonification of the laboratory bubble stream for a pump frequency of 4.8 kHz and at 200 Pa amplitude. This pressure amplitude is smaller than that used in the later sea trials, as it was found that this was the maximum insonification level before surface waves were excited on the bubble wall [24]. These surface waves caused the rising bubbles to follow a helical, rather than a vertical, path through the high-frequency transducer focus. Clearly visible are the $\omega_t + \omega_p$ and $\omega_i - \omega_p$ signals separated by approximately 600 Hz: this separation appears because the scattered signals are subjected to a Doppler shift due to the bubble movement. To facilitate the information transfer and storage, the high-frequency signal scattered from the bubble is analog-demodulated using the original imaging signal (described elsewhere [7]), and the two peaks are shifted accordingly. The demodulated and Doppler-shifted imaging signal is also evident at 300 Hz.

Fig. 4(b) records the "height" of the imaging and the sum-and-difference peaks, as the laboratory bubble stream was insonified with a pump signal of amplitude 200 Pa between 3800 and 5800 Hz in 25-Hz steps. This was the frequency interval within which the bubble resonance is known to lie. These signal "heights" were found through obtaining the power spectral densities of the returned signals and then summing the energy contained in each peak. These were then converted back to voltage measurements, as it was found that this gave the most accurate and constant signal height estimates. In summary, therefore, the crosses shown above the three peaks in Fig. 4(a) indicate this equivalent signal voltage for a single setting of the pump frequency, whilst the data in
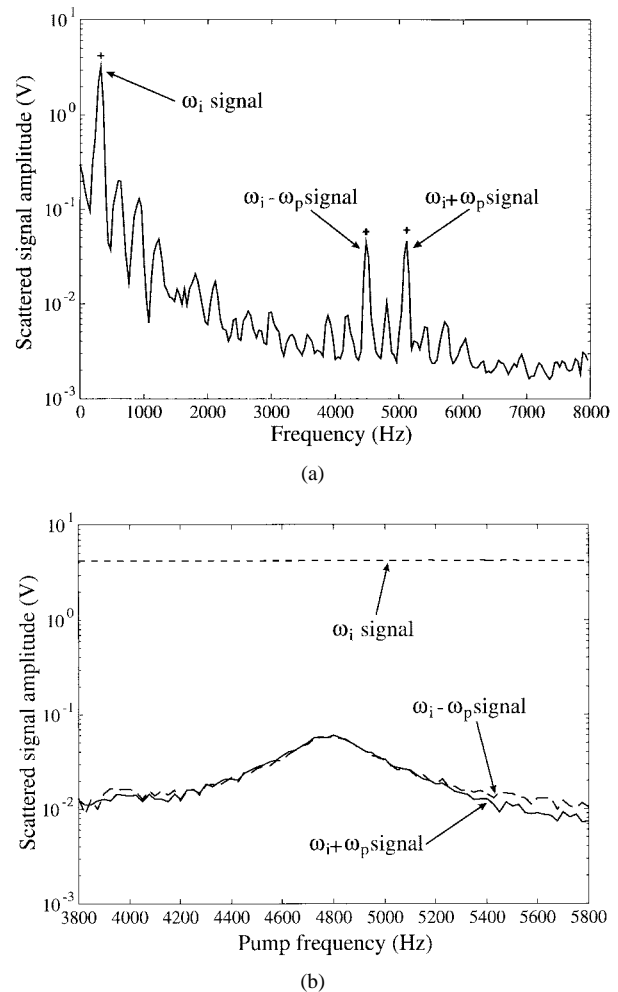

Fig. 4. (a) Typical spectrum from laboratory measurements at $\omega_p/2\pi = 4.8$ kHz. The data was insonified at a pump signal amplitude of 200 Pa, and the crosses indicate the heights of the signals after the energy summation at each of the peaks. (b) Heights of the sum-and-difference signals (unbroken and large dashes, respectively) and imaging signal (small dashes) when the stream of bubbles resonant at 4.8 kHz are insonified between 3.8 and 5.8 kHz in discrete 25-Hz steps, and at an amplitude of 200 Pa.

Fig. 4(b) shows the three signal heights over the entire range of pump signals. It is apparent that the bubbles in the stream are resonant at 4.8 kHz, with a returned signal height of 0.060 V at the location of the $\omega_i + \omega_p$ signal and 0.058 V at the $\omega_i - \omega_p$ signal. The imaging signal remains constant over the series of measurements, at a height of 4.15 V. This gives a ratio of the imaging signal to the $\omega_i + \omega_p$ signal of 36.8 dB and of 37.1 dB to the $\omega_i - \omega_p$ signal, which can be used to validate the performance of the model later on.

The second stage of the calibration involved modeling the bubble-mediated sound pressure at the receiver transducer due to the two insonifying sound field signals. The same bubble size and insonification conditions as employed in the laboratory experiments were used, for a range of bubble sizes from 600 to 800 μm insonified by a 200 Pa amplitude sine wave of frequency 4800 Hz. The results from estimating the heights of the two $\omega_i \pm \omega_p$ signals and the ω_i signal are shown in Fig. 5.

It is clear from the figure that the strength of the $\omega_i + \omega_p$ and the $\omega_i - \omega_p$ signals reach a maximum of 2.13 and 2.05 Pa,
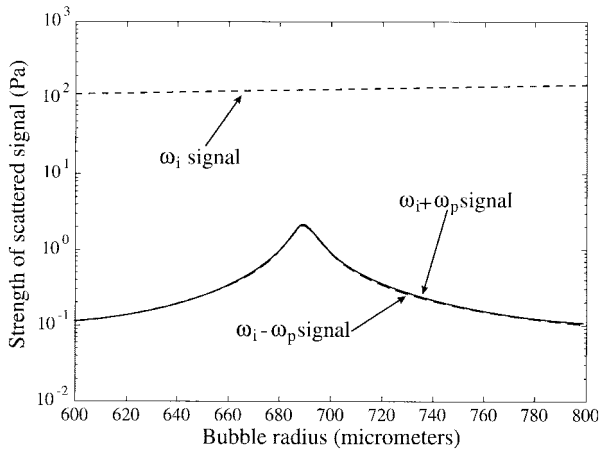
Fig. 5. Analytically derived amplitudes of the sum-and-difference signals (unbroken and large dashes, respectively) and imaging signal (small dashes) for an insonifying sound field of frequency 4.8 kHz and an amplitude of 200 Pa, over a radius range 600–800 μm.

V. OCEANIC DATA COLLECTION AND RESULTS

The equipment schematic for the oceanic trials is shown earlier. The canister comprised a 1000-mm-long × 355-mm-diameter watertight aluminium alloy cylinder, which was painted to minimize corrosion and clamped to a rigid scaffold buoy, as shown in Fig. 6. The canister contained the high-frequency projector signal power amplifier, the crystal oscillator, high-frequency receiver preamplifier, demodulator equipment, and the first of the differential amplifier pairs. The latter was included to ensure that there was no signal corruption in the passage of the returned signal along the 200-m umbilical connecting the canister to the ship-based equipment. Additionally, a temperature sensor was added to monitor the effects that the enclosed space had on the potential of the equipment to overheat.

The design of the buoy ensured that the apparatus remained stable in the water and that the focus of the transducers was at 50 cm below the surface and as remote as possible from the cylinder. This was to minimize the effect that wave-breaking events around the buoy had on the measured population. The buoy was deployed from the back of a ship and allowed to drift approximately 30 m behind the vessel. The wave events around the apparatus were continuously videotaped to allow the measured bubble population (which was recorded as a "snapshot" every 8 s) to be correlated with the surface wave activity above the sensors. The variation in wind speed and water depth were noted throughout. Additionally, a dictaphone record of the measurements and a slide film was taken, again with the time of each shot noted for later population comparisons. A frame from the video footage of the apparatus in the sea is shown in Fig. 7, relating to trial number 6, "snapshot" 4.

The tests were performed on 27 June 1997 in water that ranged in depth from 17 to 22 m and in (unseasonally high) wind speeds between 10–12 m/s, gusting at up to 16 m/s. The equipment was deployed off the Southampton coast at 50° 46.153 ′N, 1°80.911 ′W. The pump signal contained ten frequencies at 17, 28, 50, 60, 88, 110, 145, 165, 180, and 200 kHz (corresponding to resonant bubble radii of 192, 157, 64, 53, 36, 29, 22, 20, 18, and 16 μm), which were concatenated into one signal with suitable markers to speed up the data collection and storage. The storage oscilloscope was triggered by these markers to allow the separate signals to be identified in the returned waveform. The backscattered sound at each separate frequency was sampled at 500 kHz for 50 000 points, which resulted in a 1-s sample window of the bubble population over the ten output signals. The bubble population was insonified at 1000-Pa pump signal output. This is a suitably low amplitude to ensure that the small perturbation approximations inherent in the analytical model are valid (this will be discussed in the next section) and that the insonifying sound field does not affect the local population through rectified diffusion [17]).

A typical returned signal from the tests is shown in Fig. 8, for a 110-kHz pump signal frequency. To facilitate the data processing, the returned data was digitally narrow-band filtered and decimated. The frequency component of the signal

respectively, at a bubble radius of 689 μm, with a height of the scattered imaging signal of 129 Pa. The 3-dB width of the peak can also be estimated at 9.9 μm. This can be now compared with the measurements of the scattered signal from the 4800-Hz bubble stream. Comparison of the heights of the two imaging signal strengths, and consideration of the frequency responses of the preamplifier and demodulator, allow the sensitivity of the high-frequency transducer to be estimated at 8.8 μV/Pa. An additional correction to the eventual oceanic measurements will arise due to the nonmonopole scattering characteristics of the imaging beam from the comparatively large members of the laboratory bubble stream, and this will be discussed later in Section VI.

As a method of testing the validity of the model, the difference in the strengths of the imaging signal and the two sum-and-difference peaks were also calculated. The ratio of the imaging signal to the sum-and-difference terms is 35.7 and 36.0 dB, respectively, in the theoretical predictions, which results in a 1.1-dB discrepancy in both cases when compared to the experimentally measured difference shown in Fig. 4(b). This is equivalent to a 14% error in the estimates of the sum-and-difference signal pressure. If the damping was taken to arise through viscous losses alone, and the thermal and radiation effects were to be ignored (see Section III-A), the ratio of the imaging signal height to that of either combination frequency signal would be less than 1 dB, which is equivalent to a discrepancy of ∼35 dB. The off-resonance behavior of the model can itself be validated through a comparison of the two Q factors of the theoretical and experimental data. If, as a first approximation, the resonance frequency is considered to be inversely proportional to the bubble's equilibrium radius (as is the case when using Minnaert's results to relate the two parameters [25]), the Q factor of the theoretical signal heights can be estimated from the radius spread of the sum-and-difference signals divided into their resonant radius value. This gives a Q factor of 18.2, which compares very closely with the value of 17.8 measured from the experimental data.
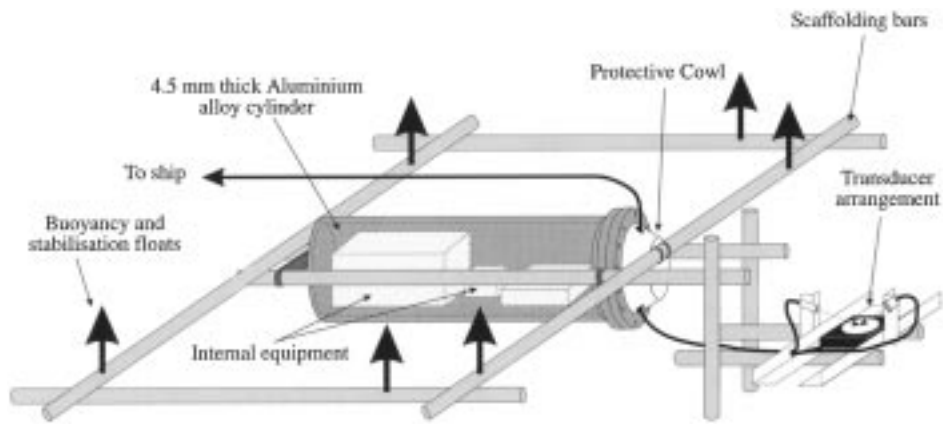
Fig. 6.   Deployment details of the watertight canister and buoy.

Fig. 7.   Frame from video record of tests, showing the sea state around the measurement buoy. The frame is from trial 6, snapshot 4.

containing the most energy (the unshifted main peak due to direct scattering of the imaging signal from the moving pump transducer itself) was then removed to improve the SNR. Thus the frequency axis shows a scale centered around 1000 Hz regardless of the value of the pump frequency. However, the absolute frequency separation of signals around this direct coupled sum-and-difference peak frequency are still maintained. Clearly visible are the two $\omega_i + \omega_p$ signals which have undergone a Doppler shift when being scattered from a moving bubble, and are located 500 Hz either side of the direct coupled signal at 1 kHz.

The analysis of the measured signal strength involved summing the energy over each of the peaks and converting this total signal energy estimate back to a voltage sum, as described earlier in keeping with the laboratory calibration tests. The energy summation was performed automatically, with often more than one bubble contributing to the total $\omega_i \pm \omega_p$ energy.

The criteria for deciding whether a signal is bubble-mediated are that there must be simultaneous peaks in the spectrum at the same frequency distance on either side of the direct coupled signal, and the signal energy of the two peaks must be within a factor of two. This analytical procedure will inevitably include some nonbubble information into the final count (which will be discussed in the next section), but will also ensure that bubbles which pass through the transducer focus for a short period of time (as most will compared with the 0.1-s sample window at each frequency) will also contribute to the total bubble count.

In total, six trials were performed on a single voyage, each comprising ten consecutive runs of the ten-frequency signal. The runs were 8 s apart, caused by the time required to transport all the data across to the PC via the GPIB interface. These results were then analyzed to get the total bubble-mediated voltage signal at both the $\omega_i + \omega_p$ and $\omega_i - \omega_p$ frequency locations. These were corrected using the estimate
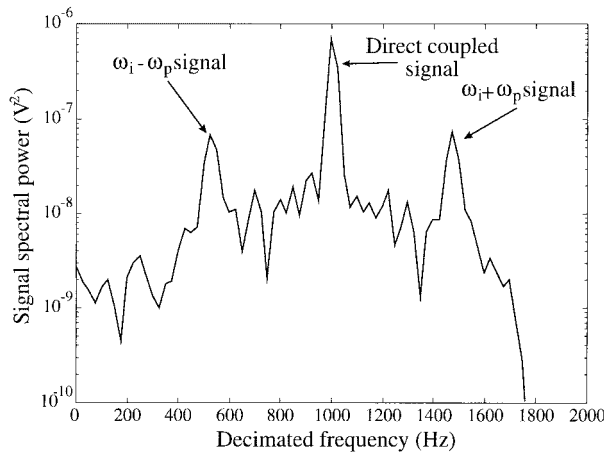
Fig. 8. Typical results from the oceanic measurements, showing the demodulated, filtered, and heterodyned frequency content for an insonifying 110-kHz pump signal. The frequency axis shows a scale centered around 1000 Hz regardless of the value of the pump frequency, although the absolute frequency separation of signals around this direct coupled sum-and-difference peak frequency are still maintained.
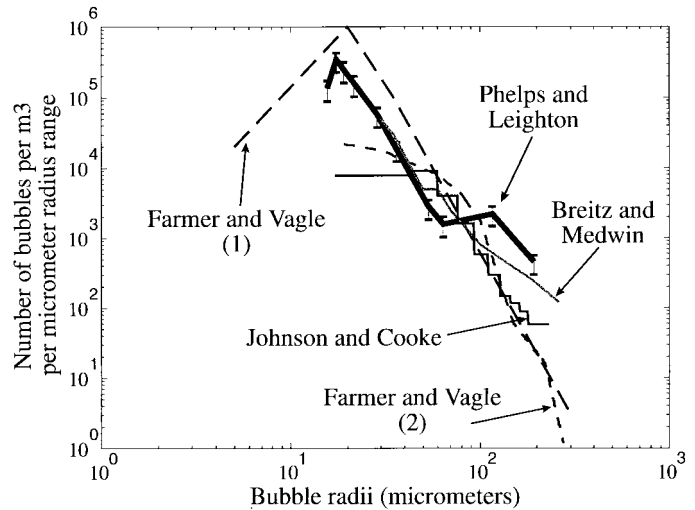

Fig. 9. Comparison of time-averaged data measured in deep water using the sum-and-difference technique (thick unbroken line), with historical estimates taken from [6], [9], [11], and [12]. The combination frequency technique is taken from trial number 6. The sources of the ascribed error margins shown for the data are detailed later.
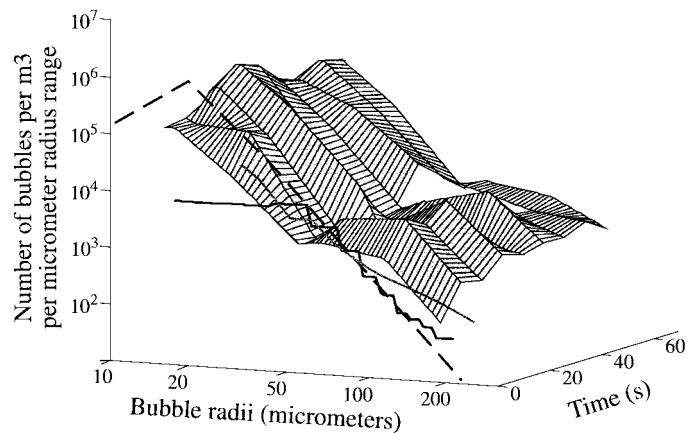

Fig. 10. Mesh plot showing the variation in bubble population over the course of the same trial as the time-averaged data shown in Fig. 9. The snapshots were collected approximately 8 s apart, and three historical measurements of the population ([6], [9] and [11]) are shown at time 0 for comparison. Signal components which return a zero count in the sample volume at a particular frequency display as white.

for the sensitivity of the receiver transducer and the measured frequency responses of the preamplifier, demodulator, and differential amplifiers to get a measured bubble sound pressure level. This was converted into the number of bubbles per micrometer radius range by dividing the estimates through by the theoretical 3-dB spreads of the $\omega_i + \omega_p$ and $\omega_i - \omega_p$ signals (this has been shown to yield an accurate estimate for the off-resonant bubble contribution [6]), and scaled to give the number per unit volume by dividing by the estimated insonification volume. The average bubble density was then calculated by averaging over the ten time samples which made up the trial, and by averaging the estimates derived from the sum-and-difference data. At smaller radii, the theoretical heights of the $\omega_i + \omega_p$ and $\omega_i - \omega_p$ signals begin to diverge, probably due to the truncation of the expanded Herring–Keller series at terms in x^2. This tends to overestimate the number of bubbles using the $\omega_i - \omega_p$ signal and underestimate the population using just the $\omega_i + \omega_p$ signal, and thus an average was used as a better indicator of the actual population. The estimated average population for the sixth trial, which is typical of the returned data, is shown in Fig. 9, compared with the historical measurements [5], [9], [11], [12].

It is apparent that the size spectrum estimated using this two-frequency technique yields a similar form to the earlier measurements, but differs slightly in several important respects. For bubbles larger than 80-μm radius, the combination frequency tests show a considerable increase in population over any of the historical studies. This may be a result of wave action against the buoy generating larger bubbles. Between 30- and 80-μm radii, the data follow the Breitz and Medwin estimates very closely down to the size resolution limit of their data collection. For bubbles smaller than 30 μm, the combination frequency population data carries on, rising to a peak of 3.4×10^5 bubbles per m^3 per micrometer radius range at 18-μm radius. This is similar to the first Farmer and Vagle data set [5], which showed a peak at a 20-μm radius of 1×10^6 bubbles per m^3 per micrometer radius range.

As the collected data consists of effective snapshots of the local bubble population, the time variation of the population can be investigated. Fig. 10 shows a mesh plot of the evolution of the population over the series of individual snapshots which made up the same trial shown averaged in Fig. 9. The mesh plot also shows three of the earlier historical measurements [5], [9], [11] at time 0 for comparison. It is evident at 24 s that a wave break event has just occurred and there is an increase in the bubble population over the entire radius range. A similar, but smaller event, is shown after 56 s. In between, the population falls off over the radius range, with a rise in the number of larger bubbles evident at 40 s. This evolving population can be matched up with breaking wave events around the apparatus monitored on the video footage, but analysis of the simultaneous acoustic and video information has not indicated clear trends. This is probably due to the

50-cm depth of the focus of the transducers. This would give a time lag between the wave breaking and the acoustic measurements, which are strongly influenced by the turbulent nature and persistence of bubbles in the subsurface sea layer.

VI. DISCUSSION

The comparison of the collected data with historical deep-water measurements needs to be justified in oceanographic terms, as clearly water depths of approximately 20 m, as used in these trials, tend to be found in coastal regions only. This can be examined using the dispersion equation [26], which relates the angular frequency of the dominant waves (σ), their wavenumber (k), and the depth of the water (d) through

$$\sigma^2 = gk \tanh(kd). \tag{7}$$

For the wave-breaking events to be classified as occurring in deep water, the presence of the sea bed must have no appreciable effect on the events on the surface, and the product kd can be assumed to be greater than unity. Thus, (7) reduces to

$$\sigma^2 = gk, \quad kd \gg 1. \tag{8}$$

Examination of the video footage taken at the time of the tests shows a dominant wave period of approximately 3.5 s. Using the deep-water approximation, (8) yields a value for the wavenumber k of 0.33 m^{-1}; the general dispersion relationship (7), solved numerically, also gives a value for k of 0.33 m^{-1}. These give a value for kd of 6.5. This calculation suggests that the presence of the sea bed has no appreciable effect on the surface wave period and that the data collected can be most closely compared with the four deep-water historical measurements detailed earlier.

The peak in the population at 18 μm is evident on each of the six trials performed. The existence of a peak in a given oceanic bubble population is a contentious point: the most recent historical population measurement using the flat plate acoustic resonator technique [12] does not show this peak, only a flattening of the number of bubbles per micrometer radius range as the radius is decreased to its minimum value of ~16 μm. However, from a consideration of the mechanisms of bubble fragmentation, a peak in the spectrum should be expected. The ambient population of small bubbles which persist over many hundreds of seconds (the so-called "old-age" population) arises though the fragmentation of larger bubbles which are caught in oceanic shear currents and the high amplitude (and therefore unstable) oscillations which follow entrainment. However, as a bubble becomes smaller, the effect of the surface tension around the wall becomes more and more important in determining its stability. For a 1-mm bubble, these Laplace surface tension forces account for around 0.1% of the internal pressure of a nonpulsating bubble at atmospheric pressure, but these rise to ~8% for a 16-μm bubble. The weaker the surface tension effects, the greater the ease by which a bubble can deform its shape from spherical, and therefore also the probability by which a shape oscillation can lead on to bubble fragmentation. Therefore, the larger the bubble, the more potent are buoyancy and

fragmentation at removing it from the population. However, every fragmentation produces a number of smaller bubbles from one fragmenting bubble; this tendency to break up decreases with decreasing size, and the smaller the bubble the stronger the Laplace forces drive it into dissolution (though stabilizing mechanisms may also have a role [4]). Logically, therefore, a maximum should exist in the old-age bubble-size distribution.

The possible sources of error in our estimates of the local bubble population can now be considered. These may arise through systematic errors in the calibration technique, measurement errors, or errors in the actual analysis of the data. To first examine errors in the calibration, it is worth noting the choice of bubble size used in the laboratory calibration of the apparatus. To scatter incident sound as a monopole source, the bubble must satisfy the following criterion:

$$k_a R_0 \ll 1 \tag{9}$$

where k_a is the wavenumber of the incident acoustic sound field. However, the scattering of the imaging sound field from the 689-μm bubbles used in the calibration tests has a $k_a R_0$ value of 2.9, which means that the scattering is not uniformly distributed with angle. The theoretical polar scattering at such a $k_a R_0$ value was modeled using the analysis of Nishi [27], which showed that the amount of acoustic energy incident on the receiver transducer angled at 90° to the imaging signal direction was 2.9 dB lower than it would be if the bubble radiated as a monopole. If no correction were made, this would translate to a 40% overestimate in the measured numbers of bubbles. As this error is systematic (and would therefore extend across the entire range of bubbles measured), it was incorporated into the conversion of signal level to number of bubbles. For the actual bubbles measured in the sea trials, the largest are those resonant at 17 kHz: these have radii of 192 μm and therefore a $k_a R_0$ value of 0.8 when considered with the imaging sound field. Using the same analysis, this would equate to only a 0.5-dB drop in the measured scattered energy over that of a monopole source, which would give a very slight underestimate of the actual population at the largest size of 6%.

To further investigate systematic calibration errors, it is necessary to evaluate how accurately the chosen pulsation model behaves. It has been demonstrated (Section IV) that our choice of model correctly incorporates the damping mechanisms for a 4.8-kHz resonant bubble, such that the relative heights of the two sum-and-difference signals are accurate to ~1 dB when compared with the scattering of the imaging signal. The actual error of 1.1 dB again equates to an overestimation of the population, of around 14%. For the small bubble sizes, the primary source of damping arises through thermal losses, which is the least well defined of the three mechanisms. The choice of incorporating this mechanism into the pulsation model by using a polytropic index to represent the compression of the gas inside the bubble is a nonexact description of the actual process [28]. However, this will not contribute a significant error into the pulsation model [7] compared to the other errors, at the small perturbation amplitudes experienced by the bubbles (as quantified below).

The divergence of the two theoretically derived sum-and-difference estimates at small bubble size is probably an artefact of the approximations made in order to solve the pulsation model analytically. The first of these approximations, that the bubble pulsations are sufficiently low amplitude to be represented in terms of a radial excursion variable (x), is the more valid. This is evident due to both the amplitude of the driving sound field and the fact that the divergence in the two signals occurs for the smaller bubbles rather than the larger, where the relative amplitude of the pulsations would be higher. This approximation was evaluated explicitly using a numerical solution to the Herring–Keller equation, which is described elsewhere [29]. This yielded radius/time plots of the bubble pulsations when driven at 1 kPa, and both the largest bubbles (of equilibrium radius 192 μm) and smallest (of 16 μm) were examined when driven at their resonance frequencies of 17 and 200 kHz, respectively. It was found that the maximum departure of the bubble radius from its equilibrium value was 14% for the larger bubble, and only 10% for the smaller, which are both sufficiently small for the $x \ll 1$ condition to still be valid. The divergence in the two sum-and-difference signals is due in large part to the truncation of the terms at x^2 in the expanded Herring–Keller formulation. However, the error in the population estimate is minimized through averaging the two results derived from considering the $\omega_i + \omega_p$ and $\omega_i - \omega_p$ signals separately.

The estimate of the insonification volume does not suffer from the drawbacks inherent in earlier tests [7], where the high-frequency transducers were necessarily placed such that their focus was in the near field of each to minimize the insonification volume in the high population environment. The current layout is such that the volume estimate error is thought to be within 20% of the actual insonification volume.

Errors in the measurement of the bubble population are harder to quantify. The analysis of Feuillade [30] mathematically evaluates the effects of mutual interaction between bubbles which pulsate in phase (which, because of the π phase shift at resonance, represents only a partial description of the total dynamics). This formulation suggests that at the low void fractions measured here ($\sim 1.6 \times 10^{-4}$%) the effects of multiple bubble interaction are negligible when compared with other sources of error. However, his analysis considers not just the total void fraction but the effect of peaks in the bubble population size distribution. For the data presented here, the peak in the population at 18 μm contains 3.4×10^5 bubbles per micrometer radius per m^3. This equates to a measurement of 160×10^3 bubbles per m^3 when the adjustment for the 3-dB span of 0.46 μm is removed, equivalent to an interbubble spacing of 19 mm. This is over 1000 times larger than the bubbles' equilibrium radii, and therefore sufficiently large to ensure that mutual excitation effects are negligible.

A potential further source of error may arise through attenuation of the high-frequency beams due to the bubble population. This can be examined using the formulation of Commander and Prosperetti [22]. Although this is only accurate for estimating the attenuation of signals whose frequencies are far removed from the resonances of the members of the population, the number of bubbles resonant at 1 MHz is almost certainly very small. The attenuation of the 1-MHz beams due to the presence of the total bubble cloud can be estimated at 0.19 dB/m, which represents a change in the imaging pressure amplitude over the 32-cm signal path length of under 1%. This is indeed marginally lower than the attenuation in bubble-free water of 0.22 dB/m at 20 °C [31], a value which is the same for both seawater and freshwater and is therefore already included for in the calibration.

The protocol for the analysis of the data, where a peak is counted as a bubble signal when there is a simultaneous peak in the $\omega_i + \omega_p$ and $\omega_i - \omega_p$ signals and their relative energies are approximately the same, would overpredict the *number* of bubbles measured. However, as the sum-and-difference data taken from a genuine bubble can be orders of magnitude higher than these peaks due to the noise, the averaged total energy will not be affected to any great degree.

VII. Conclusions

The text details the application of a combination frequency sizing technique to oceanic bubble measurements. These are compared with existing historical measurements of bubbles taken near the surface in oceanographically deep water and at high wind speeds. The results show a similar form to the earlier measurements but demonstrate a maximum in the bubble population at 18-μm radius. This compares with one historical measurement by Farmer and Vagle [5] which itself shows a maximum at 20 μm, although these combination frequency estimates give a bubble count at 18 μm which is only a third of the count at 20 μm found by the earlier workers.

Acknowledgment

References

[1] G. M. Wenz, "Acoustic ambient noise in the ocean: spectra and sources," *J. Acoust. Soc. Amer.*, vol. 34, pp. 1936–1956, 1962.

[2] D. K. Woolf, "Bubbles and the air-sea transfer velocity of gases," *Atmosphere-Ocean*, vol. 31, pp. 451–474, 1993.

[3] S. Thorpe, "On the clouds of bubbles formed by breaking wind-waves in deep water, and their role in air-sea gas transfer," *Philos. Trans. R. Soc. London A*, vol. 304, pp. 155–210, 1982.

[4] T. G. Leighton, *The Acoustic Bubble.* London, U.K.: Academic, 1994.

[5] D. M. Farmer and S. Vagle, "Waveguide propagation of ambient sound in the ocean-surface bubble layer," *J. Acoust. Soc. Amer.*, vol. 86, pp. 1897–1908, 1989.

[6] A. D. Phelps and T. G. Leighton, "Measurement of bubble populations near the sea surface using combination frequencies: Adaptation and calibration of device between two sea trials," in *Natural Physical Processes Associated with Sea Surface Sound*, T. G. Leighton, Ed. Southampton, U.K.: Univ. of Southampton, 1997, pp. 198–210.

[7] A. D. Phelps, D. G. Ramble, and T. G. Leighton, "The use of a combination frequency technique to measure the surf zone bubble population," *J. Acoust. Soc. Amer.*, vol. 101, pp. 1981–1989, 1997.

[8] W. K. Melville, E. Terrill, and F. Veron, "Bubbles and turbulence under breaking waves," in *Natural Physical Processes Associated with Sea Surface Sound*, T. G. Leighton, Ed. Southampton, U.K.: Univ. of Southampton, 1997, pp. 135–146.

[9] B. D. Johnson and R. C. Cooke, "Bubble populations and spectra in coastal waters; A Photographic approach," *J. Geophys. Res.*, vol. 84, no. C7, pp. 3761–3766, 1979.

[10] A. L. Walsh and P. J. Mulhearn, "Photographic measurements of bubble populations from breaking waves at sea," *J. Geophys. Res.*, vol. 92, no. C13, pp. 14553–14565, 1987.

[11] N. Breitz and H. Medwin, "Instrumentation for in situ acoustical measurements of bubble spectra under breaking waves," *J. Acoust. Soc. Amer.*, vol. 86, pp. 739–743, 1989.

[12] D. M. Farmer and S. Vagle, "Bubble measurements using a resonator system," in *Natural Physical Processes Associated with Sea Surface Sound*, T. G. Leighton, Ed.   Southampton, U.K.: Univ. of Southampton, 1997, pp. 155–162.

[13] V. L. Newhouse and P. M. Shankar, "Bubble sizing using the nonlinear mixing of two frequencies," *J. Acoust. Soc. Amer.*, vol. 75, pp. 1473–1477, 1984.

[14] J. Y. Chapelon, P. M. Shankar, and V. L. Newhouse, "Ultrasonic measurement of bubble cloud size profiles," *J. Acoust. Soc. Amer.*, vol. 78, pp. 196–201, 1985.

[15] P. M. Shankar, J. Y. Chapelon, and V. L. Newhouse, "Fluid pressure measurement using bubbles insonified by two frequencies," *Ultrasonics*, vol. 24, pp. 333–336, 1986.

[16] D. Koller, Y. Li, P. M. Shankar, and V. L. Newhouse, "High speed bubble sizing using the double frequency technique for oceanographic applications," *IEEE J. Oceanic Eng.*, vol. 17, pp. 288–291, 1992.

[17] T. G. Leighton, A. D. Phelps, and D. G. Ramble, "Bubble detection using low amplitude multiple acoustic techniques," in *Proc. 3rd Eur. Conf. Underwater Acoustics*, J. S. Papadakis, Ed.   Crete, Greece: FORTH-IACM, 1996, pp. 1143–1148.

[18] E. A. Zabolotskaya and S. I. Soluyan, "Emission of harmonic and combination-frequency waves by air bubbles," *Sov. Phys. Acoust.*, vol. 18, pp. 396–398, 1973.

[19] A. I. Eller, "Damping constants of pulsating bubbles," *J. Acoust. Soc. Amer.*, vol. 47, pp. 1469–1470, 1970.

[20] C. Herring, "Theory of the pulsations of the gas bubble produced by an underwater explosion," Rep. No. 236, *OSRD*, 1941.

[21] J. B. Keller and M. Miksis, "Bubble oscillations of large amplitude," *J. Acoust. Soc. Amer.*, vol. 68, pp. 628–633, 1980.

[22] K. W. Commander and A. Prosperetti, "Linear pressure waves in bubbly liquids: comparison between theory and experiments," *J. Acoust. Soc. Amer.*, vol. 85, pp. 732–746, 1989.

[23] R. Clift, J. R. Grace, and M. E. Weber, *Bubbles, Drops, and Particles.* New York: Academic, 1978.

[24] A. D. Phelps and T. G. Leighton, "High resolution bubble sizing through detection of the subharmonic response with a two frequency technique," *J. Acoust. Soc. Amer.*, vol. 99, pp. 1985–1992, 1996.

[25] M. Minnaert, "On musical air-bubbles and the sounds of running water," *Phil. Mag.*, vol. 16, pp. 235–248, 1933.

[26] P. H. LeBlond and L. A. Mysak, *Waves in the Ocean.* New York: Elsevier, 1989.

[27] R. Y. Nishi, "The scattering and absorption of sound waves by a gas bubble in a viscous liquid," *Acustica*, vol. 33, pp. 65–74, 1975.

[28] A. Prosperetti, L. A. Crum, and K. W. Commander, "Nonlinear bubble dynamics," *J. Acoust. Soc. Amer.*, vol. 83, pp. 502–514, 1988.

[29] A. D. Phelps, "Characterisation of the subharmonic response of a resonant bubble using a two frequency technique," Ph.D. dissertation, Univ. of Southampton, U.K., 1995.

[30] C. Feuillade, "The attenuation and dispersion of sound in water containing multiply interacting air bubbles," *J. Acoust. Soc. Amer.*, vol. 99, pp. 3412–3430, 1996.

[31] L. E. Kinsler, A. R. Frey, A. B. Coppens, and J. V. Sanders, *Fundamentals of Acoustics.* Singapore: Wiley, 1982.

Andy D. Phelps, photograph and biography not available at the time of publication.

Timothy G. Leighton, photograph and biography not available at the time of publication.